JOURNAL OF AIRCRAFT
Vol. 45, No. 2, March–April 2008

Transport Aircraft Wake Influenced by a Large Winglet and Winglet Flaps

Alexander Allen[*] and Christian Breitsamter[†]
Technical University of Munich, 85747 Garching, Germany

DOI: 10.2514/1.32787

Detailed flowfields of a wind-tunnel investigation are discussed presenting the wake vortex development and evolution in the near field and extended near field behind a four-engined large transport aircraft model fitted with a large winglet. The tests use a half-model of 1:32 scale focusing on the high-lift case of a typical approach configuration at a Reynolds number of 0.5×10^6 based on the wing mean aerodynamic chord and at an angle of attack of 7 deg. Flowfields are carefully inspected by advanced hot-wire anemometry at seven crossflow planes up to 5.6 spans downstream of the model. Based on the measured time-dependent velocity components, the wake flowfield is analyzed by distributions of mean velocity and vorticity, turbulence intensities, and spectral densities. The near-field wing vortex sheet is dominated by seven main vortical structures, namely the winglet vortex, the wing tip vortex, the outboard flap vortex, the outboard and inboard nacelle vortices, and the vortices shed at the wing-body junction and the horizontal tail plane. In the extended near field, these vortices roll up and merge to form the remaining rolled-up vortex. The deflection of winglet flaps produce additional vortices influencing the wing tip near field and enhancing the overall merging process. Especially for the cases with asymmetrical flap deflection, the remaining rolled-up vortex shows a significant narrowband concentration of turbulent kinetic energy which may result in an amplification of inherent far-field instabilities.

Nomenclature

AR = aspect ratio
b = wing span, m
b_0 = main vortex pair distance, m
C_D = drag coefficient
C_L = lift coefficient, $2L AR/(\rho U_\infty^2 b^2)$
C_m = pitching moment coefficient
$\bar{c}$ = wing mean aerodynamic chord, m
f = frequency, Hz
k = reduced frequency, $fb/(2U_\infty)$
L = lift, N
$Re_{\bar{c}}$ = Reynolds number, $U_\infty \bar{c}/\nu$
r_c = vortex core radius, m
$S_{u'}^N$ = power spectral density of u' normalized with $(\Delta k U_\infty)/(\overline{u'^2}(b/2))$
Tu_x, Tu_y = axial, lateral, vertical turbulence intensity, $\sqrt{\overline{u'^2}}/U_\infty$, $\sqrt{\overline{v'^2}}/U_\infty$,
Tu_z = $\sqrt{\overline{w'^2}}/U_\infty$
U_∞ = freestream velocity, m/s
u, v, w = axial, lateral, and vertical velocities, m/s
$\bar{u}$, $\bar{v}$, $\bar{w}$ = mean axial, lateral, and vertical velocities, m/s
u', v', w' = fluctuation part of u, v, and w, m/s
x, y, z = coordinates in x, y, and z direction, m
x^* = nondimensional distance in x direction, x/b
y^*, z^* = nondimensional distances in y and z direction, $2y/b$, $2z/b$
α = aircraft angle of attack, deg
δ = winglet flap deflection, deg
ν = kinematic viscosity, $\mathrm{m^2/s}$
ξ = nondimensional axial vorticity, $\bar{\omega}_x b/(2U_\infty)$
ρ = density, $\mathrm{kg/m^3}$
τ^* = nondimensional time, $x^* 16 C_L/(\pi^4 AR)$
$\bar{\omega}_x$ = mean axial vorticity component, $(d\bar{w}/dy - d\bar{v}/dz)$, 1/s

Subscripts

d = dominant
l, u = lower, upper

Introduction

As a result of the increasing air traffic and the growing difficulties in expanding airports and runways, the maximum capacities at major airports around the world is almost reached. To counteract this development, aircraft size is increased. The minimum distance between two aircraft on approach, takeoff, and en route is primarily driven by the maximum takeoff weight and therewith by the size of the two aircraft [1,2]. The Federal Aviation Administration in the United States and the Civil Aviation Authority in Europe regulate the separation distances. These distances are estimated as conservative to account for the varying behavior of the vortices under different atmospheric conditions [3]. Under the constraint of keeping today's safety level, a reduction of the separation distances would lead to a relief at hub airports to meet the requirements of growing air traffic. The new generation of very large transport aircraft can only disburden the bottleneck if their separation distances are not increased with respect to their increase in seating capacity.

In the past, the wake vortical structure and related issues have been intensively investigated [4–7]. It is well known that the trailing wake of a lifting body rolls up into a pair of strong counter-rotating longitudinal vortices that persist for many body dimensions downstream. The vortex strength is proportional to the bound circulation or body lift, and hence, for steady flight conditions, this is approximately proportional to the weight of the generating aircraft. An aircraft encountering a vortex wake can experience sudden upwash, downwash, or rolling along with increased structural loads, depending on its position and orientation with respect to the wake. Rapid changes of attitude or heavy disturbances of trimmed flight conditions are especially dangerous near the ground.

Received 13 June 2007; revision received 19 October 2007; accepted for publication 19 October 2007.

[*] Diplom-Ingenieur, Master of Science, Research Engineer, Institute of Aerodynamics. Member AIAA.

[†] Privatdozent Doktor-Ingenieur, Chief Scientist, Institute of Aerodynamics. Associate Fellow AIAA.

Several integrated research projects address the wake vortex physics and means of wake vortex alleviation [8–10]. The wake vortex evolution and development is studied using various experimental and numerical methods [11,12]. Tests are conducted on generic models as well as on detailed transport aircraft models. Wind-tunnel, towing tank, and catapult experiments give specific and complementary data resulting in a sound description of the structure of the wake vortices progressing downstream. Also, a lot of effort is put into tracking and identification of wake vortices using ground-based and in-flight measurements [13]. Flight tests have been performed using triangular lidar measurements to observe and reveal the development of a wake generated by an aircraft under real meteorological conditions [14]. Also, computational methods, including, e.g., vortex filament methods, Reynolds-averaged Navier–Stokes computations, and large eddy simulations, are widely used to describe all stages of the wake vortex development [15–17]. The models employed depend strongly on the treatment of turbulent and unsteady quantities. Experimental studies have shown the importance of unsteady effects on the wake vortex formation and evolution [18].

Precise tracking or prediction of wake vortex locations under all weather conditions is beyond the range of current technology. Therefore, many research activities concentrate on alleviating the wake vortex hazard by modifications of wing geometry and/or wing loading. Strategies to minimize the wake vortex hazard concentrate either on a low vorticity vortex (LVV) design or on a quickly decaying vortex (QDV) [11]. The LVV design reduces the wake vortex hazard by enhancing the dispersion of the vorticity field. It is aimed on the generation of wake vortices with larger core size and smaller swirl velocities at the core radius after roll up is completed. Also, an optimum wing load distribution may minimize the induced rolling moment for a following aircraft [19]. The alteration of the circulation distribution of the wake generating wing can be obtained by using differential flap settings. It has been shown that a wing with an outboard partially deflected flap and an inboard fully deflected flap produces, at least in the extended near field, a smaller induced rolling moment than a wing with a standard flap setting [20]. An enhanced vortex decay may be achieved by promoting three-dimensional instabilities by means of active or passive devices [21–23]. An active system uses periodic oscillations of control surfaces to introduce the desired perturbations leading to the breakup of the trailing vortices into vortex rings [24]. A concept using a generic wing with oscillating winglet flaps was investigated in water tank experiments [25]. Because a multiple vortex system shows instabilities which can grow more rapidly, passive devices aim to promote these kinds of instabilities through the deliberate production of single vortices in addition to those coming from the wing tip and the flap edge [11,21,26]. The efficiency of these concepts depends on the persistence of separate vortex pairs which is determined by configurational details of the aircraft wing.

The results presented herein concentrate on the vortex wake of a large transport aircraft featuring a large winglet fitted with a lower and upper winglet trailing-edge flap. The flowfield development is characterized by axial vorticity distributions, turbulence intensity patterns, and spectral densities. The investigation is aimed at documenting in detail the wake vortex development in the near field and extended near field and analyzing the influence of winglet and two winglet flaps on the rolled-up vortex characteristics.

Experimental Setup

The investigation was conducted in the wind-tunnel facility C of the Institute of Aerodynamics (AER) at the Technical University of Munich (TUM) using a detailed large transport aircraft configuration and employing advanced hot-wire anemometry.

Wind Tunnel

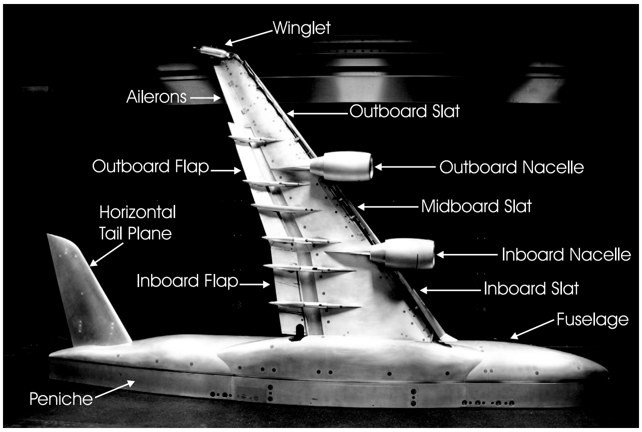

Fig. 1 Half-model of large transport aircraft installed in test section of wind-tunnel C.

The wind-tunnel C is of closed–return type and has a long-range test section of 21 m length, which covers a wake distance of approximately 5.6 spans downstream of the model. The wind tunnel has a cross section of 1.8 × 2.7 m. The ceiling is adjustable to control the axial pressure gradient along the test section. The turbulence level at the nozzle exit is less than 0.5%.

Model

A 1:32 scaled half-model of a typical large transport aircraft is used, Fig. 1. The model has a wing semispan of 1.242 m ($AR = 8.0$), a wing mean aerodynamic chord of 0.362 m, and a fuselage length of 2.119 m. The model is made of aluminum and is equipped with fully adjustable flaps, slats, ailerons, and horizontal tail plane. The experiments concentrate on the approach configuration with the setting of the high-lift devices as listed in Table 1. The horizontal tail plane setting is -10.0 deg. The engine nacelles are designed as through-flow nacelles.

The wake flowfield is investigated for the configuration with an "original" large winglet as well as for a "new" large winglet. The latter replaces the original winglet to install two trailing-edge flaps influencing the wake vortex evolution. The new winglet is made of titanium with the same dimensions as the original large winglet, Fig. 2. To supply sufficient space for the driving components of the flap actuator system, a slightly thicker airfoil (NACA65A012) than for the original cambered winglet with a thickness of approximately 11% is chosen. The winglet is equipped with a lower and upper moveable trailing-edge flap, the deflection of which is statically or dynamically up to $\delta = \pm 20$ deg. The flaps can be moved in phase or with 180 deg phase shift, i.e., flaps are deflected in opposite direction. A positive deflection $\delta > 0$ means an outboard movement of the flaps and hence some small local lift increase. The possible oscillation frequency is up to 100 Hz provided by an electronic servo motor. The housing of this motor is manufactured as a tilted cylinder at the wing tip lower side, Fig. 2. The influence of this wing tip cylinder on the wake flowfield is discussed in the results section.

Measurement System and Test Conditions

A triple-wire probe operated by a multichannel constant temperature anemometer system is used to measure time series of axial, lateral, and vertical velocities. The tungsten wires are platinum plated and have a diameter of 5 μm and a length of approximately 1.25 mm. The wires are arranged perpendicular to each other to achieve best angular resolution. An additional temperature probe is employed to correct anemometer output voltages if ambient flow temperature varies. A sampling rate of 3000 Hz (Nyquist frequency 1500 Hz), a low-pass filter frequency of 1000 Hz and a sampling time of 6.4 s were chosen. The sampling time corresponds to 19,200

Table 1 High-lift device settings

	Slat	Flap	Aileron
Inboard	26.5 deg	26.0 deg	5.0 deg
Midboard	26.5 deg	——	——
Outboard	30.0 deg	26.0 deg	5.0 deg

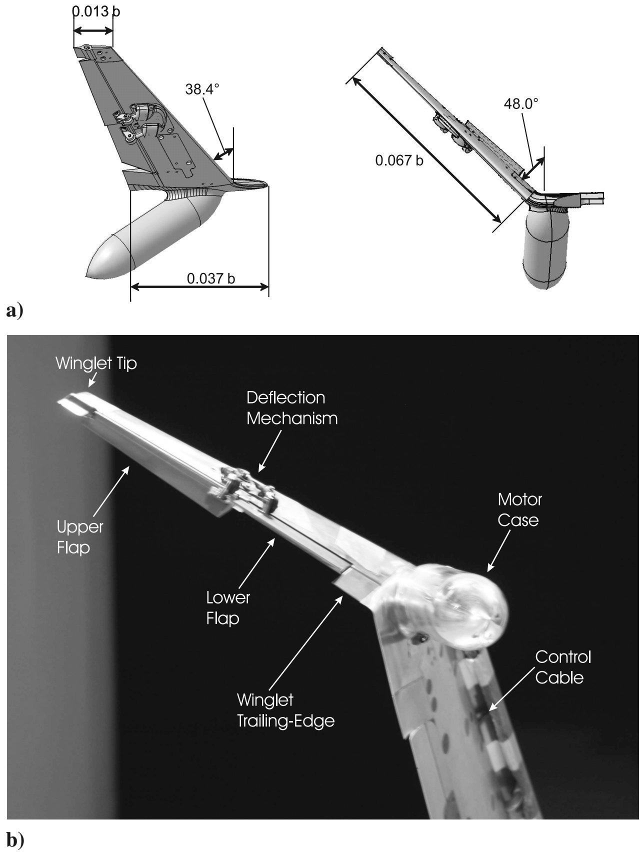

Fig. 2 New large winglet with trailing-edge flaps: a) geometry, b) elements.

values per wire and survey point. The signals are digitized with 16 bit precision through a 16 channel simultaneous sampling A/D converter. The sampling parameters were achieved by preliminary tests to ensure that all relevant flowfield phenomena are detected. The anemometer output signals are converted into time-dependent velocity components u, v, and w using a lookup table previously obtained from the velocity- and angle-dependent calibration of the hot-wire probe [27]. Based on statistical error evaluation, accuracies are in the range of 1% for mean quantities, 2.5% for rms quantities (turbulence intensities), and 4% for spectral densities [18,27].

The investigations are all performed at a velocity of $U_\infty = 25\ \mathrm{m/s}$ corresponding to a Reynolds number of $Re_{\bar{c}} = 0.5 \times 10^6$ based on the wing mean aerodynamic chord. The angle of attack for the original winglet configuration is chosen to be $\alpha = 7.0$ deg and for the new winglet configuration $\alpha = 6.5$ deg to keep the lift coefficient constant at $C_L = 1.43$. The decrease in angle of attack of $\Delta\alpha = 0.5$ deg to keep the lift coefficient constant is mainly due to the influence of the wing tip tilted cylinder housing the servo motor of the moveable winglet flaps. The flow around the inclined cylinder increases the local effective angle of attack in the winglet region. The lift coefficient was determined by force measurement using an external six-component balance. Measurement accuracies related to the underfloor six-component wind-tunnel balance are 0.025% based on maximum loads of the balance load cells. Conducting half-model tests, maximum allowable loads refer to 1500 N in the axial direction, ±3000 N in the normal direction, and ±700 Nm in pitching moment. Thus, minimum detectable loads for axial force, normal force, and pitching moment are 0.38 N, 1.5 N, and 0.18 Nm, respectively. Thus, an accuracy in drag coefficient, lift coefficient, and pitching moment coefficient of $\Delta C_D = 0.0028$, $\Delta C_L = 0.011$, and $\Delta C_m = 0.0037$ is obtained for the present test. Inspecting the surface flow with tufts showed attached flow is present on the wing and horizontal tail plane and therefore no transition strips were attached to the model.

The model is positioned on the tunnel floor with the wing reference point (WRP) at 2.8 m downstream of the nozzle exit, and the wing tip pointing upward (Fig. 1). The WRP is the position of the trailing edge at the winglet tip at an angle of attack of $\alpha = 0.0$ deg, where $x^* = 0$. A peniche of 0.095 m height is used to raise the model fuselage above the wind-tunnel floor boundary layer. The model wing box is attached to the driven shaft of a computer controlled model support located below the test section floor, allowing a precise angle of attack setting. The test section is further equipped with a three-axis probe traversing system giving minimum steps of ±0.2 mm in axial, lateral, and vertical directions. The vortex wake is measured in seven crossflow planes orientated perpendicular to the freestream direction at distances $x^* = x/b = 0.02$, 0.37, 1.0, 2.0, 3.0, 4.0, and 5.6 downstream of the WRP. In regions of high flow gradients, i.e., in the areas of vorticity layers and vortex cores, the survey points are closely spaced with a relative grid resolution of 0.004 in spanwise and 0.006 in vertical direction based on the wing span. Outside these regions, the relative spacing is gradually enlarged to 0.024 laterally and 0.036 vertically. Regarding the susceptibility of vortical structures to intrusive measurements, it was found that the presence of the hot-wire probe has no marked influence on the wake vortex formation and evolution [11].

Results and Discussion

Regarding the downstream development, a vortex wake can be divided into four main regions: 1) the near field, $x/\bar{c} \approx 1$, which is characterized by the formation of highly concentrated vortices shed at all surface discontinuities; 2) the extended near field, $x^* \leq 10$, where the wake roll-up process takes place, and the merging of dominant vortices (flap edge, wing tip) occurs, leading gradually to two counter-rotating vortices; 3) the far field, $10 \leq x^* \leq 100$, where the wake is descending in the atmosphere and linear instabilities emerge; 4) the decay region, $x^* > 100$, where fully developed instabilities cause a strong interaction between the two vortices until they collapse. Here, results for the near field and extended near field are shown. The downstream stations are marked by the nondimensional distance x^* and the characteristic time $\tau^* = x^* 16 C_L/(\pi^4 A\!\!R)$. The latter number includes lift coefficient and aspect ratio to compare results of different tests and configurations with reference to an elliptic lift distribution. The flowfields are presented as contour plots of nondimensional axial vorticity ξ and vertical turbulence intensity Tu_z.

Baseline Configuration

To quantify the influence of the new winglet on the wake vortex flowfield, a detailed investigation is conducted using both the original winglet and the new winglet, the latter without deflection of the winglet flaps.

Original Winglet

The nondimensional axial vorticity distribution and turbulence intensities of the crossflow plane at $x^* = 0.37$, $\tau^* = 0.011$, are shown in Fig. 3. The main near-field vortices are marked by the corresponding acronyms and their peak vorticity levels are stated. Note, that the vorticity levels $-1.0 < \xi < 1.0$ are blanked in all those figures to clarify the positions of dominating vortices. Turbulence intensity levels of $Tu_z < 0.02$ are also blanked to emphasize the vortex sheet emanating from the wing more clearly.

Seven main vortices can be identified, namely from outboard to inboard: the winglet vortex (WLV), the wing tip vortex (WTV), the outboard nacelle vortex (ONV), the outboard flap vortex (OFV), the inboard nacelle vortex (INV), the horizontal tail plane vortex (HTV), and the merged inboard flap vortex and wing-fuselage vortex (IFV/WFV), Fig. 3a. Note that the HTV and the IFV/WFV have negative vorticity and are therefore counter-rotating in comparison to the other five vortices. The horizontal tail plane is adjusted for negative lift due to trimmed flight and, therefore, the HTV exhibits negative vorticity. The negative circulation gradient in the wing-fuselage region leads to the counter-rotating WFV. Further, the vortex sheet emanating from the wing trailing edge and the vortex sheet shed at the horizontal tail plane are clearly shown. The two strongest vortices based on peak

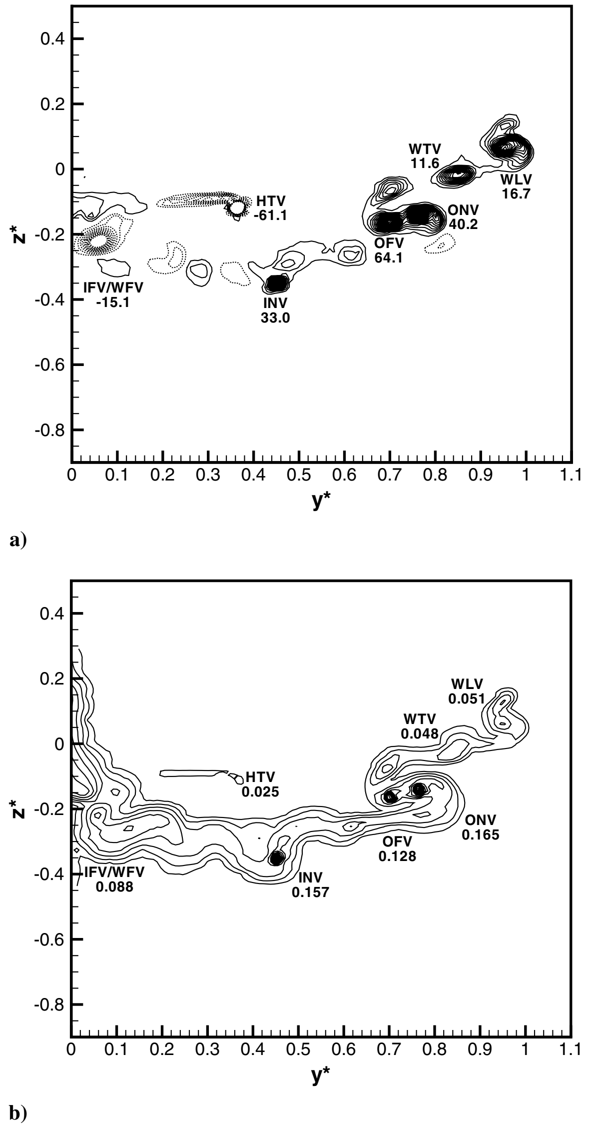

Fig. 3 Contour plots of nondimensional axial vorticity ξ and turbulence intensity Tu_z distributions for the configuration with original winglet at $x^* = 0.37$, $Re_{\bar{c}} = 0.5 \times 10^6$: a) ξ; solid lines, positive values; dashed lines, negative values; $-10 \leq \xi \leq 50$; $\triangle\xi = 1$; b) Tu_z; $0.02 \leq Tu_z \leq 0.2$, $\triangle Tu_z = 0.01$.

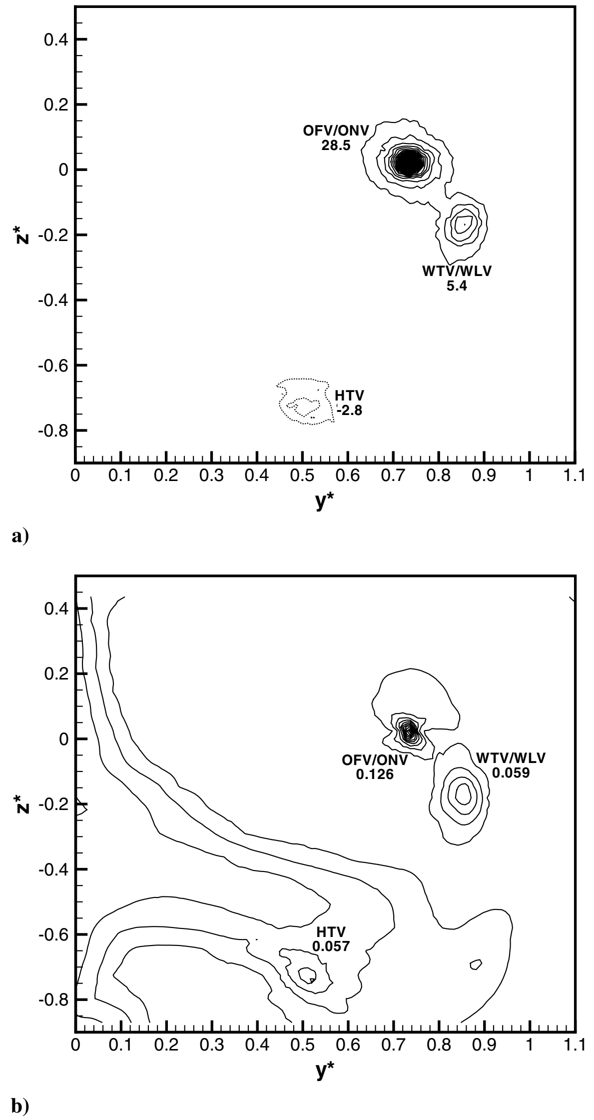

Fig. 4 Contour plots of nondimensional axial vorticity ξ and turbulence intensity Tu_z distributions for the configuration with original winglet at $x^* = 5.6$, $Re_{\bar{c}} = 0.5 \times 10^6$: a) ξ; solid lines, positive values; dashed lines, negative values; $-10 \leq \xi \leq 50$; $\triangle\xi = 1$; b) Tu_z; $0.02 \leq Tu_z \leq 0.2$; $\triangle Tu_z = 0.01$.

vorticity levels are the ONV and the OFV with the latter clearly being the strongest of all such distinct vortices. The maximum peak vorticity level of the OFV is associated with the highly loaded outboard flap. The relatively high vorticity level of the ONV is caused by the inclined ring profile of the nacelle subject to the crossflow caused by the swept wing. The "s-like" shape of the vortex sheet in that region indicates that the two vortices have rotated around each other by approximately 180 deg. Local turbulence maxima are found in the regions of high vorticity, Fig. 3b. These turbulence maxima are evoked by the strong velocity gradient and streamline curvatures in the vortex crossflow areas and by the inflection in the radial profiles of the retarded axial core flow. Also, several less pronounced vortices indicated by smaller vorticity levels are present in between the six dominating wing vortices. These smaller vortices are caused by flow separation at slat horns, flap track fairings, and other geometric discontinuities of the wing. The fuselage wake is visible by a large region of increased turbulence intensity close to the plane of symmetry ($y^* \approx 0$, $-0.4 < z^* < 0.3$). This region is larger than the fuselage diameter caused by the upwash of the inclined fuselage and by the downwash of the wing, which moves the fuselage turbulence wake from its original position resulting in a vertically stretching of the fuselage turbulence sheet.

Progressing downstream to $x^* = 5.6$, $\tau^* = 0.164$, three main vortices remain at this station of the extended near field, Fig. 4. The strongest one is formed by the merging of the OFV with the ONV, and the second one by the merging of the WTV with the WLV. The HTV is also still visible, but its peak vorticity level is strongly reduced. Because of the induced velocity fields of the OFV/ONV and the WTV/WLV on the HTV, the latter sinks faster than the other two vortices. The IFV/WFV and the INV have fed vorticity to other vortical structures which will be explained later. In comparison to Fig. 3, the WTV/WLV has rotated around the OFV/ONV by approximately 270 deg with the peak vorticities clearly decreasing. The corresponding vortex sheets are linked, which means that merging of the WTV/WLV with the OFV/ONV begins. The ratio of core size to the distance of the two vortices is already below the critical value of 0.2 related to the start of three-dimensional vortex merging at higher Reynolds number [28]. Again, increased turbulence levels are attributed to the positions of the main vortices, Fig. 4b. The two strongest vortices are not influenced by the enlarged region of the fuselage wake, whereas the HTV is now fully embedded in this area.

New Winglet

The measurements were repeated for the new winglet with the winglet flaps being not deflected ($\delta_l = \delta_u = 0$ deg). Axial vorticity

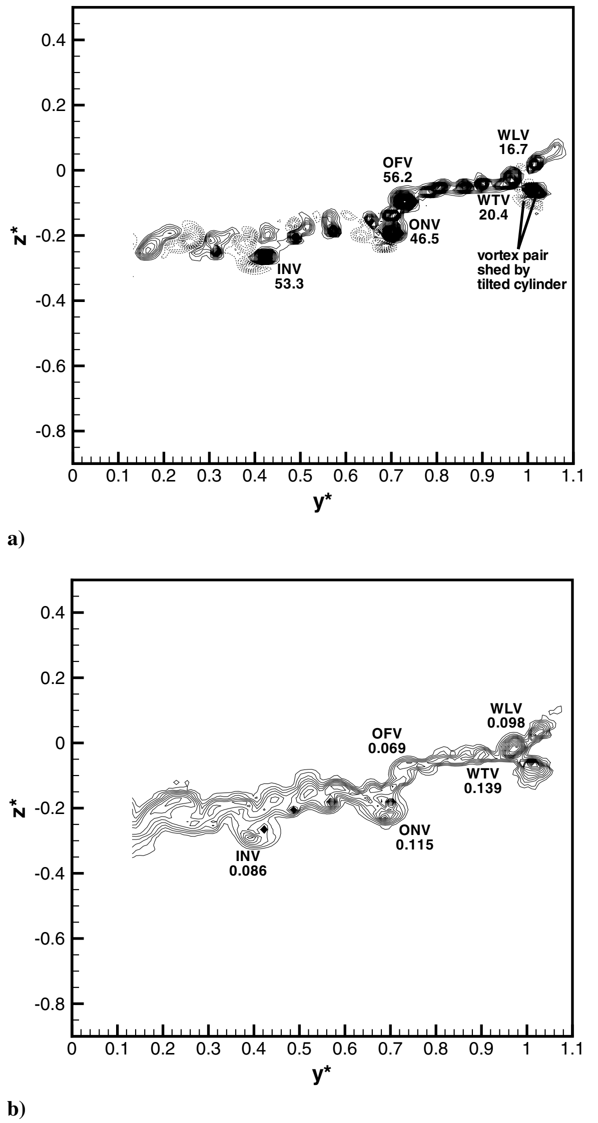

Fig. 5 Contour plots of nondimensional axial vorticity ξ and turbulence intensity Tu_z distributions for the configuration with new winglet at $x^* = 0.02$, $Re_{\bar{c}} = 0.5 \times 10^6$: a) ξ; solid lines, positive values; dashed lines, negative values; $-10 \leq \xi \leq 50$; $\triangle\xi = 1$; b) Tu_z; $0.02 \leq Tu_z \leq 0.2$; $\triangle Tu_z = 0.01$.

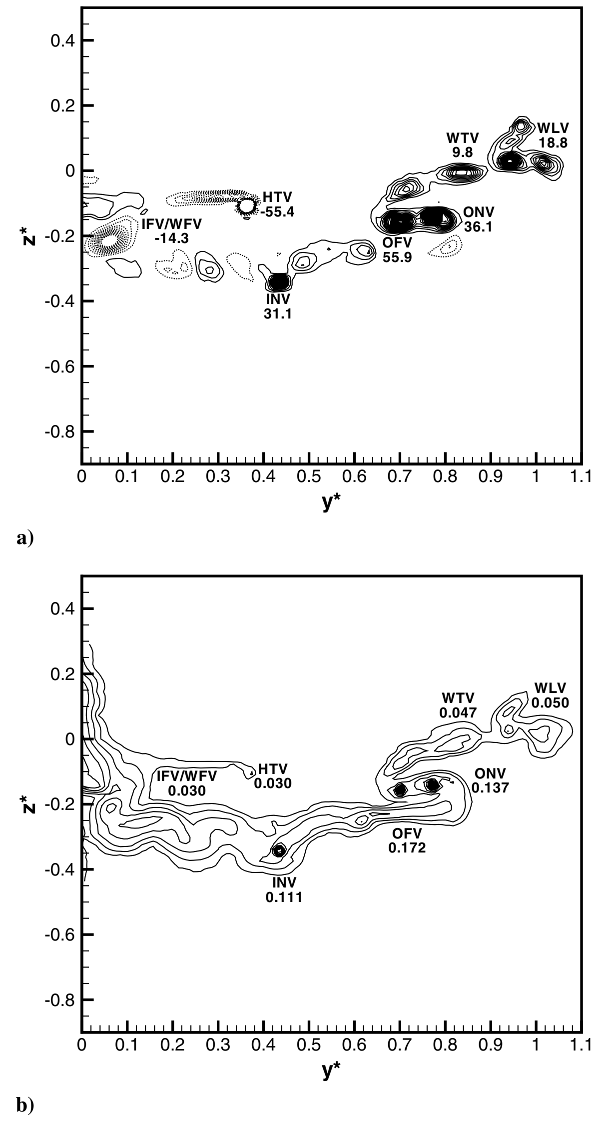

Fig. 6 Contour plots of nondimensional axial vorticity ξ and turbulence intensity Tu_z distributions for the configuration with new winglet at $x^* = 0.37$, $Re_{\bar{c}} = 0.5 \times 10^6$: a) ξ; solid lines, positive values; dashed lines, negative values; $-10 \leq \xi \leq 50$; $\triangle\xi = 1$; b) Tu_z; $0.02 \leq Tu_z \leq 0.2$; $\triangle Tu_z = 0.01$.

and turbulence intensity fields are investigated for a station close to the wing trailing edge at $x^* = 0.02$, $\tau^* = 0.0006$, Fig. 5. Because of the presence of the fuselage, it is not possible to measure at positions $y^* < 0.13$, which is why the WFV/IFV is missing. As the measuring plane is upstream of the horizontal tail plane, the HTV and the associated vortex sheet is also not present. Here, five dominating vortices can be seen, namely, the WLV, WTV, OFV, ONV, and INV. They are accompanied by further vortices indicated by lower peak vorticity levels. These vortices are caused by the geometry details of the high-lift wing configuration as mentioned previously. In addition, a counter-rotating vortex pair located outboard of the WTV can be identified in the wing tip area ($y^* = 1.02$, $z^* = -0.05 \div -0.01$). This vortex pair is caused by the tilted cylinder on the lower side of the new winglet. It will quickly merge with the WLV. The turbulence intensity distribution highlights the nacelle wake flow as bulges of increased fluctuation levels at approximately $y^* = 0.4$, $z^* = -0.3$ and $y^* = 0.7$, $z^* = -0.2$. Just outboard of the bulge caused by the outboard nacelle, a jump in the turbulence sheet can be observed. This kink is caused by the outer edge of the outboard flap. Inboard of this station, the flow has a stronger downwash due to the flaps being deflected at 26 deg. Outboard the downwash is smaller because the aileron deflections are set to 5 deg (Table 1). At the wing tip area, the vortex sheet of the new large winglet and the wake of the tilted cylinder can be recognized by increased turbulence intensities.

Comparing axial vorticity and turbulence intensity fields of the baseline and new winglet configuration at $x^* = 0.37$, $\tau^* = 0.011$ (cf. Figs. 3 and 6), some differences are found in the wing tip area. The peak vorticity and turbulence intensity levels differ slightly due to changes in the outboard wing loading. Note that the lift coefficient is kept constant. Differences in the wake near field between new and original winglet are expected due to the wake of the tilted cylinder and to a minor degree because of the change in the airfoil of the new winglet. Apart from these differences, the overall flowfield development is the same regarding the six dominating vortices and the s-like shape in the turbulence intensity field, indicating the rotation of ONV and OFV around their roll-up center.

Moving to $x^* = 1.00$, $\tau^* = 0.029$, the WTV has merged with the OFV and ONV, Fig. 7. This situation is different compared with the baseline configuration where the WTV merges with the WLV first. The "v-like" shaped vorticity pattern of the wing tip area (cf. Fig. 6, $y^* = 0.9 \div 1.1$, $z^* = 0 \div 0.15$), including three vortical centers, rolls up into the WLV. Here, it is still separated from the main vortex (OFV/ONV/WTV) but merging is already in progress. Thus, five main vortices are present at $x^* = 1.00$, with the merged OFV/ONV/WTV exhibiting the highest peak vorticity. Compared with the

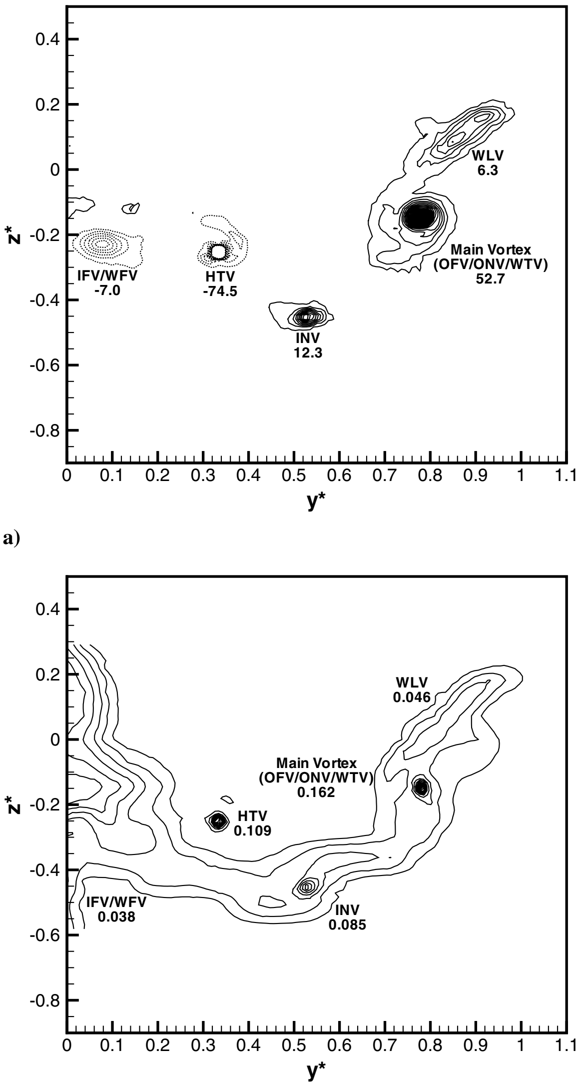

a)

b)

Fig. 7 Contour plots of nondimensional axial vorticity ξ and turbulence intensity Tu_z distributions for the configuration with new winglet at $x^* = 1.0$, $Re_{\bar{c}} = 0.5 \times 10^6$: a) ξ; solid lines, positive values; dashed lines, negative values; $-10 \leq \xi \leq 50$; $\triangle\xi = 1$; b) Tu_z; $0.02 \leq Tu_z \leq 0.2$; $\triangle Tu_z = 0.01$.

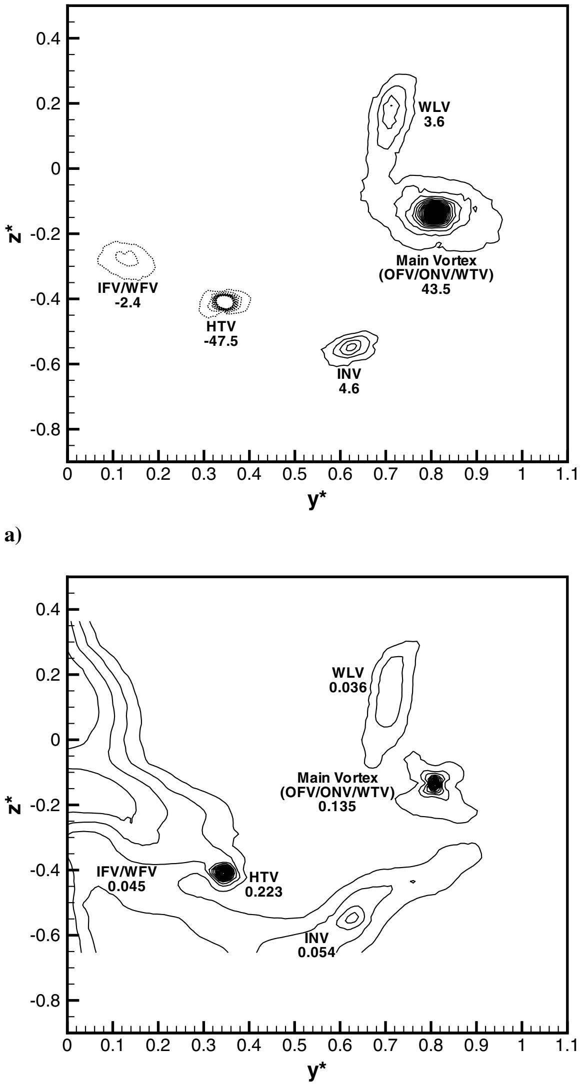

a)

b)

Fig. 8 Contour plots of nondimensional axial vorticity ξ and turbulence intensity Tu_z distributions for the configuration with new winglet at $x^* = 2.0$, $Re_{\bar{c}} = 0.5 \times 10^6$: a) ξ; solid lines, positive values; dashed lines, negative values; $-10 \leq \xi \leq 50$; $\triangle\xi = 1$; b) Tu_z; $0.02 \leq Tu_z \leq 0.2$; $\triangle Tu_z = 0.01$.

upstream station, the peak vorticity levels of all main vortices are reduced as their core diameters have increased. Local maxima of turbulence intensities are found for the main vortex, the INV, and the HTV. At $x^* = 1.00$, the HTV is completely rolled up. At $x^* = 2.00$, $\tau^* = 0.059$, all vortices have rotated counterclockwise around the roll-up center, which is located close to the position of the main vortex (OFV/ONV/WTV), Fig. 8. Vorticity is fed from the WLV to the main vortex during merging. The vortex core diameters become enlarged and the peak vorticity levels decrease further. The HTV is now embedded in the turbulence field from the wing-fuselage area, weakening its peak vorticity. Progressing further downstream, the counterclockwise rotation of the vortices continues and peak vorticity levels diminish, except for the main vortex, which is stated by the field distributions at $x^* = 3.00$, $\tau^* = 0.088$, Fig. 9. The increase in the peak vorticity level of the main vortex is due to the merging with the WLV. The predominant portion of the WLV vorticity has now been fed into the main vortex. The turbulence intensity field substantiates that the main vortex becomes the remaining rolled-up vortex of the entire wing vortex sheet. The HTV still loses a large amount of energy caused by the interaction with the area of higher turbulence intensity created by the fuselage wake. At $x^* = 4.00$, $\tau^* = 0.117$, the peak vorticity level of the IFV/WFV has decreased beyond the cutoff value of -1 and, therefore, it is no longer marked, Fig. 10. Peak values of WLV and INV are also reduced further, both in vorticity and turbulence intensity. The main vortex and the HTV are clearly marked by local maxima of turbulence intensities.

Focusing on the furthest downstream crossflow plane at $x^* = 5.6$, $\tau^* = 0.164$, two distinct vortices remain, namely, the main rolled-up vortex and the HTV, Fig. 11. The WLV can still be detected as an artifact with a position corresponding to a rotation of about 270 deg around the main vortex. Compared with the baseline configuration, a somewhat different vorticity field has developed. Two distinct vortices are present for both configurations, but the WLV is much weaker for the configuration with new winglet as for the one with original winglet. For the configuration with original winglet, the WTV merges with the WLV far upstream causing a higher WLV peak vorticity level from the very beginning, whereas for the configuration with new winglet, the WTV is fed into the OFV/ONV. Therefore, the main vortex (OFV/ONV/WTV) has a slightly higher peak vorticity than the OFV/ONV of the configuration with original winglet. Also, the peak vorticity of the HTV indicates a higher negative level.

Figure 12 summarizes the downstream development of nondimensional axial peak vorticity $\xi_{\max}$, vortex core radius r_c/b,

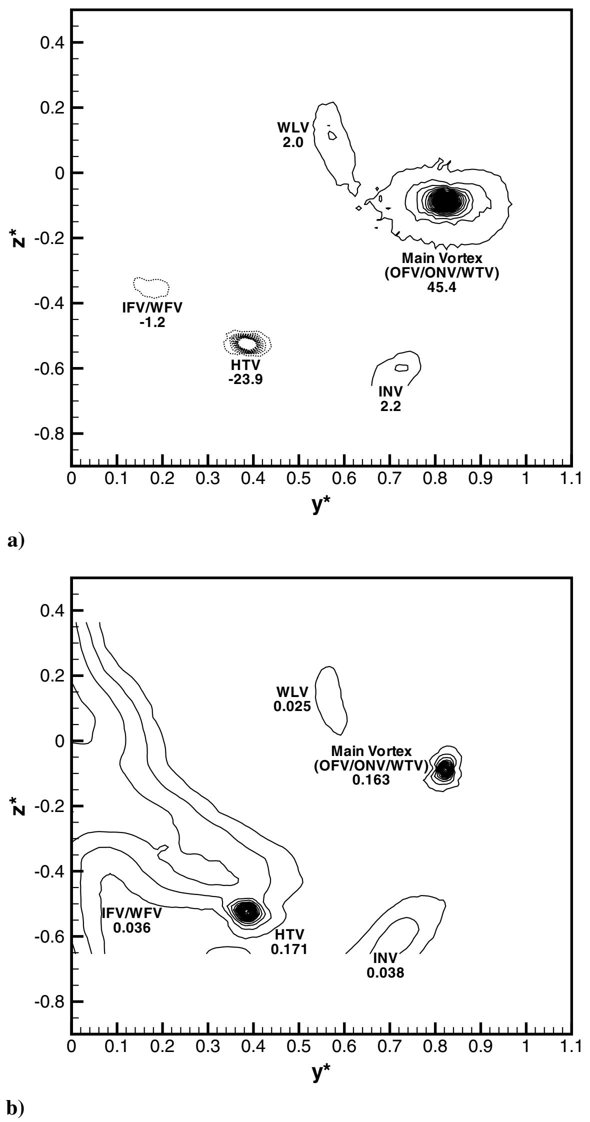

Fig. 9 Contour plots of nondimensional axial vorticity ξ and turbulence intensity Tu_z distributions for the configuration with new winglet at $x^* = 3.0$, $Re_{\bar{c}} = 0.5 \times 10^6$: a) ξ; solid lines, positive values; dashed lines, negative values; $-10 \leq \xi \leq 50$; $\triangle\xi = 1$; b) Tu_z; $0.02 \leq Tu_z \leq 0.2$; $\triangle Tu_z = 0.01$.

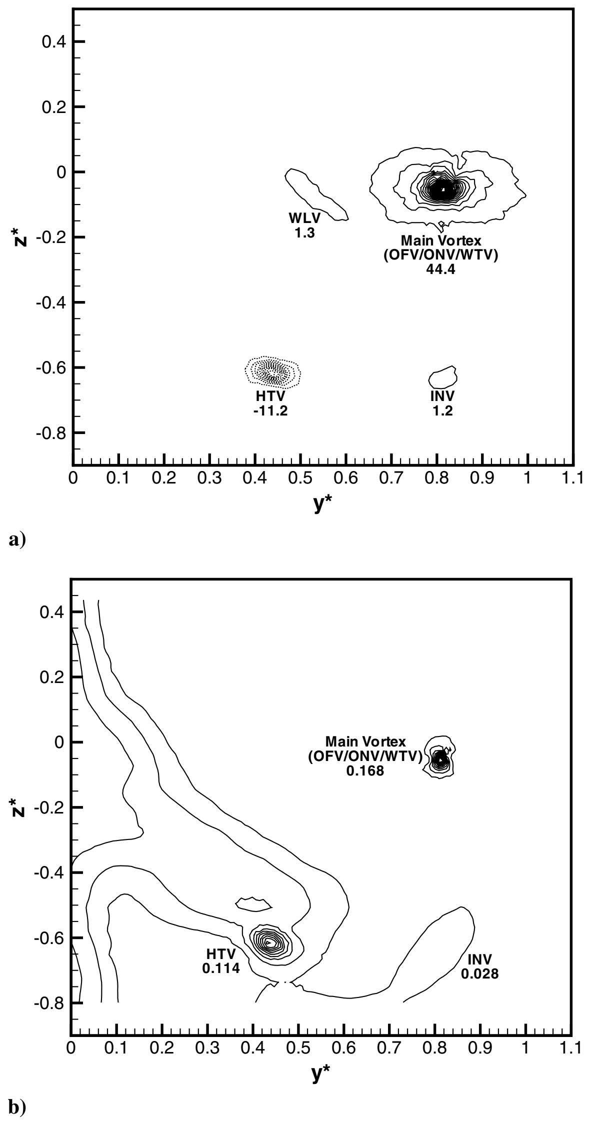

Fig. 10 Contour plots of nondimensional axial vorticity ξ and turbulence intensity Tu_z distributions for the configuration with new winglet at $x^* = 4.0$, $Re_{\bar{c}} = 0.5 \times 10^6$: a) ξ; solid lines, positive values; dashed lines, negative values; $-10 \leq \xi \leq 50$; $\triangle\xi = 1$; b) Tu_z; $0.02 \leq Tu_z \leq 0.2$; $\triangle Tu_z = 0.01$.

axial velocity deficit $U_\infty - \bar{u}_{\min}/U_\infty$, and peak turbulence intensities $Tu_{x,y,z_{\max}}$ for the main vortex as function of nondimensional distance x^* and time τ^*. These results were obtained on measuring grids with identical spatial resolution. Figure 12a illustrates the decay in peak vorticity for both the main vortex and the HTV due to turbulent diffusion $(d\xi/d\tau^*|_{\text{Main Vor.,Orig.}W.} = 42.2;\ \ d\xi/d\tau^*|_{\text{Main Vor.,New}W.} = 167.4)$. As explained before, the different levels in peak vorticity during the near-field decay depends on the merging of dominant vortices forming the main vortex. At the station furthest downstream, the peak vorticity value for both winglets is almost equal as the overall lift is kept constant. The decay rate of the HTV is clearly higher, showing only minor differences for the two winglet configurations. Here, the decay process is mainly influenced by the interaction with the highly turbulent fuselage wake. The development in the outer vortex core radius is significantly different for the two winglet geometries. This core radius is defined as distance from the vortex center with zero crossflow velocity to the radial point of maximum crossflow velocity. The original winglet configuration shows an almost constant vortex core radius with an increase from $x^* = 4.0$ to $x^* = 5.6$, whereas the new winglet configuration exhibits upstream a significant increase in vortex core size from $x^* = 1.0$ to $x^* = 3.0$ followed by a sudden drop progressing downstream. The strong increase in vortex core size is associated with the turbulent merging of dominant vortices [28]. Such merging processes are evident at $x^* \approx 5.6$ for the configuration with original winglet (merging of WTV/WLV with OFV/ONV) and at $x^* \approx 3.0$ for the configuration with new winglet (merging of WLV with OFV/ONV/WTV). After roll up of the vorticity sheets, the outer vortex core radius decreases to some extent. The axial velocity deficit shown in Fig. 12c illustrates a lower deficit for the new winglet configuration up to $x^* = 4.0$; thereafter, the deficit increases to approximately 11%. For the original winglet configuration, a decrease in the velocity deficit up to 8% can be seen over the entire downstream distance. This axial velocity deficit is a characteristic feature of the trailing vortices reflecting the retarded axial velocity due to the wing boundary layers and local trailing-edge flow separation. Figure 12d presents the peak turbulence intensities of all three velocity components. A good match between the two winglet configurations is found for the axial component Tu_x, whereas the new winglet configuration exhibits higher turbulence intensities for the lateral and vertical component Tu_y and Tu_z. At $x^* = 5.6$, such peak turbulence intensities reach levels between 12 and 18%.

Deflected Winglet Flaps

Measurements are performed with both symmetric and asymmetric static flap deflections at a maximum deflection angle

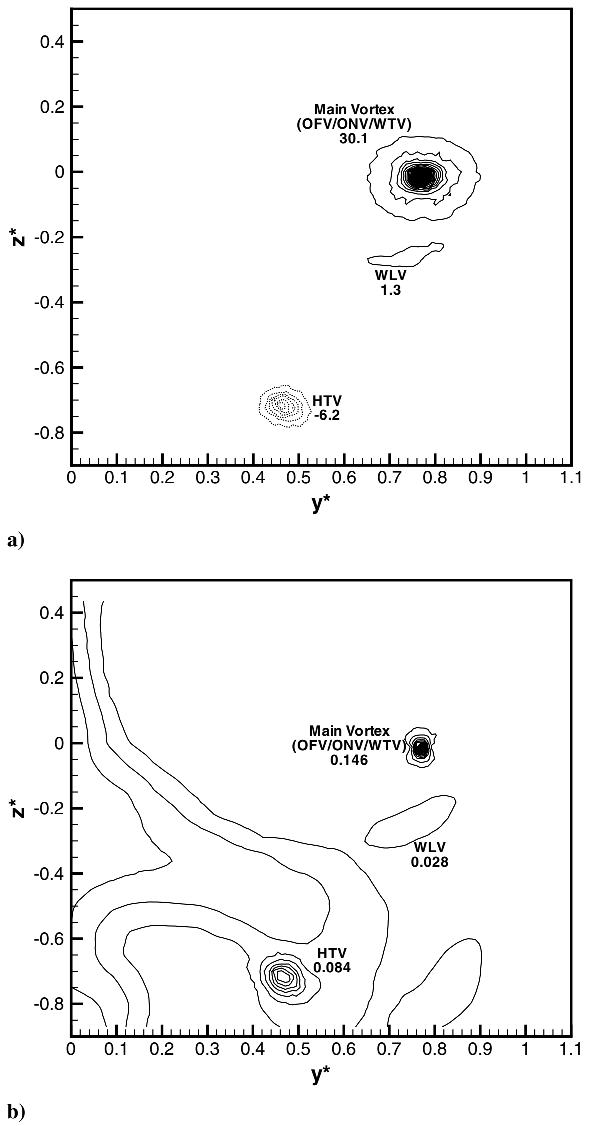

Fig. 11 Contour plots of nondimensional axial vorticity ξ and turbulence intensity Tu_z distributions for the configuration with new winglet at $x^* = 5.6$, $Re_{\bar{c}} = 0.5 \times 10^6$: a) ξ; solid lines, positive values; dashed lines, negative values; $-10 \le \xi \le 50$; $\triangle\xi = 1$: b) Tu_z; $0.02 \le Tu_z \le 0.2$; $\triangle Tu_z = 0.01$.

of $\delta = 20$ deg. Only the planes at $x^* = 0.37$ and $x^* = 5.6$ were inspected, and results are compared with those obtained for the new winglet configuration without flap deflection. Four cases are examined as listed in Table 2. Note that the case name depends on the direction of the lower flap deflection. Lift and pitching moment coefficients stay almost constant at asymmetric deflections of lower and upper flaps, i.e., flaps are deflected opposite at same nominal deflection angle. The increase in the drag coefficient is about 1.0%. The change in the aerodynamic coefficients is also given in Table 2. Regarding following investigations, the winglet flaps are also intended for active influencing of the wake flowfield. Any change of the overall forces and moments is an important issue, as the horizontal tail plane cannot be moved at such high frequencies as planned for the winglet flaps to keep the aircraft in a steady flight condition.

Vorticity Contours at $x^* = 0.37$

Close behind the winglet trailing-edge, regions of positive and negative vorticity caused by deflected winglet flaps exist. Because of the merging of the vortical structures, only regions of positive vorticity remain at $x^* = 0.37$.

The results for the case with symmetrical inboard deflection ($\delta_l = -20$ deg, $\delta_u = -20$ deg) are depicted in Fig. 13b. The WLV exhibits a significantly higher peak vorticity than without deflection and the vorticity distribution in the area of the winglet has changed. The WTV is connected to the WLV, which can also be seen in the turbulence intensity distribution. Comparing Fig. 13b with Fig. 13a clearly illustrates that the WTV and WLV start to merge, rather than the WTV with the OFV/ONV. The peak vorticity levels for the ONV and OFV are increased, which is the case for all configurations with deflected winglet flaps. The symmetrical outboard deflection ($\delta_l = +20$ deg, $\delta_u = +20$ deg, Fig. 13c) shows that the WLV peak vorticity is reduced to a value which is somewhat lower than for the baseline configuration, whereas the WTV peak level is close to the one of the baseline case. The vortices in the region of the winglet do not appear to be as stretched as for the symmetrical inboard case. The vorticity part belonging to the winglet is broadened significantly in comparison to the configuration without flap deflection. In case of the symmetrically inboard deflected flaps, this region has nearly disappeared (cf. Fig. 13b). This change in the vorticity pattern is due to the winglet shedding vorticity at an angle of incidence which is locally diminished or increased by the deflected flaps. For the symmetrical outboard deflection, the OFV shows the highest peak vorticity level of all cases.

The asymmetrical inboard case ($\delta_l = -20$ deg, $\delta_u = +20$ deg, Fig. 13d) demonstrates that the WLV has a higher peak vorticity level compared with the baseline case, as known already from the symmetrical inboard deflection. Also, the WTV is connected by a vorticity sheet to the WLV, as found for all other cases with flap deflection, representing a significant difference to the baseline configuration. Inverting the flap deflection leads to the asymmetrical outboard case ($\delta_l = +20$ deg, $\delta_u = -20$ deg, Fig. 13e). Both the WLV and the WTV have approximately the same peak vorticity as for the symmetrical outboard case, which is slightly lower than for the baseline configuration. Here, the ONV shows the highest peak vorticity of all cases with deflected flaps. Just as for the case with symmetrical outboard deflection, the vortices in the winglet region are squeezed together. Consequently, the deflection of the lower flap changes the vortex formation in the wake near-field plane far more than the upper flap. In all cases, the OFV and the ONV showed higher peak vorticity levels relative to the baseline configuration. The WLV exhibits higher peak vorticities for the inboard deflection cases and lower ones for outboard deflections, whereas the WTV is characterized by lower peak vorticities for all cases.

Vorticity Contours at $x^* = 5.6$

The remaining rolled-up vortex is called OFV/ONV, as the merging of the WTV and WLV cannot be proven by measurements of crossflow planes between $x^* = 0.37$ and $x^* = 5.6$. Considering the inboard symmetrically deflected flaps, the peak vorticity for the remaining vortex is significantly higher (57%) than for the baseline configuration. It is thought that the WTV and WLV have completely merged with the OFV/ONV, Fig. 14b. The shape and size of the vortex does not differ markedly from the baseline configuration, neither in vorticity nor in turbulence intensity distribution. The symmetrical outboard deflection case is quite similar to the symmetrical inboard one, Fig. 14c. Again, the WLV is not evident and the peak vorticity of the remaining vortex is 41% higher than for the configuration without flap deflection. Regarding the asymmetrical inboard and outboard case, the peak vorticity of the remaining vortex is increased by 54 and 46%, respectively, in comparison to the baseline case, Figs. 14d and 14e. Again, the overall vorticity distribution shows no significant change compared with the other cases.

The results of the cases with winglet flap deflections at station $x^* = 5.6$ are included in Fig. 15, presenting the downstream development of the main vortex by axial peak vorticity, vortex core radius, and peak turbulence intensity again obtained on measuring grids with identical spatial resolution. Winglet flap deflection results in an increase in peak vorticity, whereas the vortex core radius decreases. In addition, the peak turbulence intensities of the vortex core area increased in their level by approximately 4%. These data

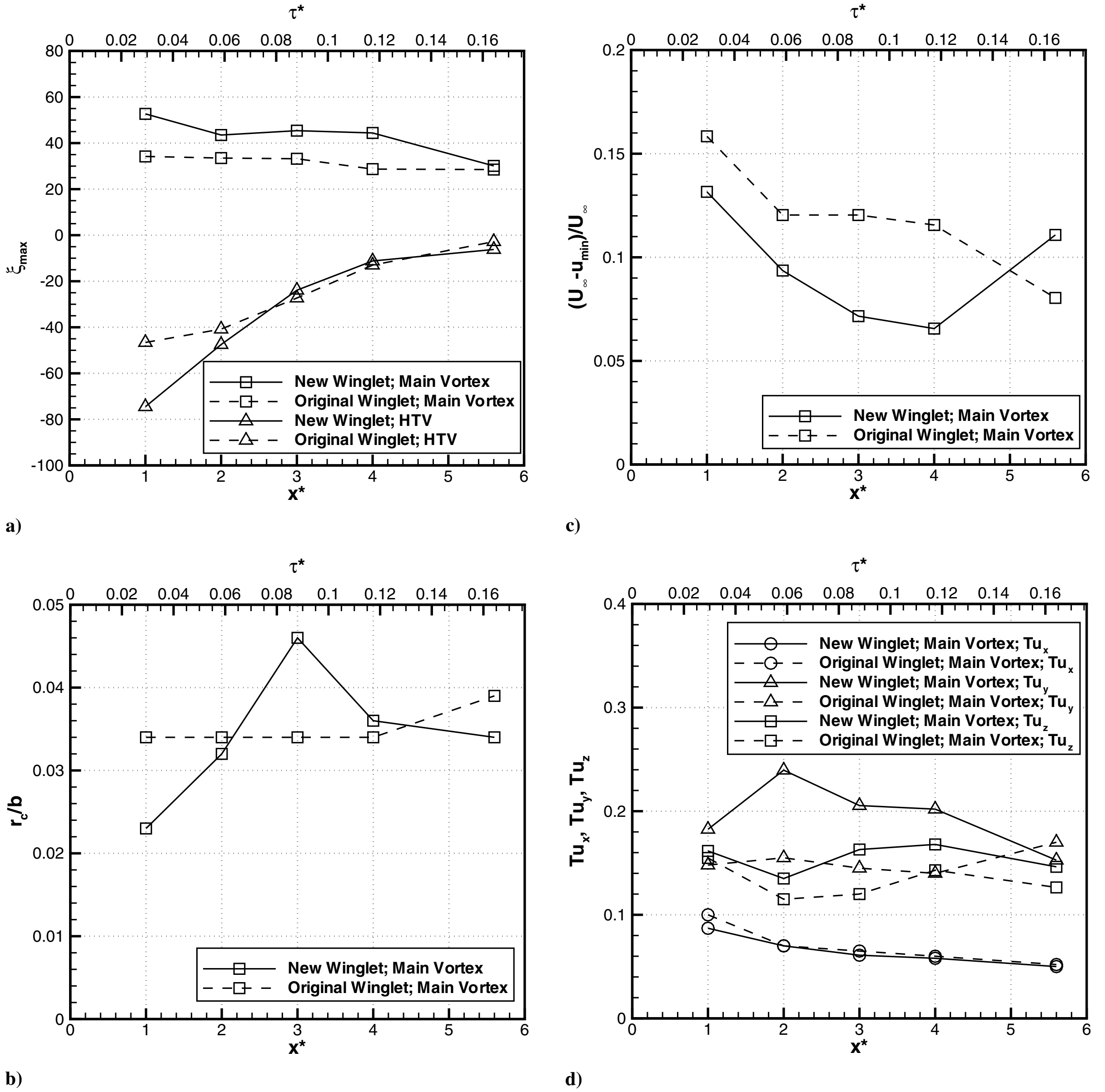

Fig. 12 Development of flowfield variables for both baseline configurations between $x^* = 1.0$ and $x^* = 5.6$, $Re_{\bar{c}} = 0.5 \times 10^6$: a) $\xi_{\max}$ for the main vortex and the HTV, b) r_c/b for the main vortex, c) $U_\infty - \bar{u}_{\min}/U_\infty$ for the main vortex, d) $Tu_{x,\max}$, $Tu_{y,\max}$, and $Tu_{z,\max}$ for the main vortex.

substantiate that the deflection of the winglet flaps markedly enhances the merging process to form the remaining rolled-up vortex.

Spectral Densities

Power spectral densities of the axial velocity fluctuations are evaluated for the core regions at $x^* = 5.6$ to detect spectral peaks associated with inherent instability mechanisms (Fig. 16a). The spectral densities are calculated using linear band averaging with 1024 frequency bands and plotted as function of reduced frequency k. The spectral densities are presented in nondimensional form for the baseline configuration, as well as for all cases with deflected winglet flaps. The latter exhibit distinct spectral peaks at reduced frequencies of $k_d = 0.1 \div 0.2$, whereas the baseline configuration does not show such narrowband concentrations of turbulent kinetic energy. The dominant reduced frequency k_d is lower for the cases with the lower flap deflected outboard and the spectral peaks are higher for asymmetrical flap deflection compared with the symmetrical one.

The presence of instability mechanisms propagating along the vortex wake in the streamwise direction can lead to a relevant distortion of the vortex, accelerating its decay and dispersion. Typically, long- and short-wave instabilities occur. The most significant long-wave instability for a vortex pair is the Crow instability [29].

Table 2 Cases with deflected winglet flaps

Case name	δ_l	δ_u	ΔC_L, %	ΔC_D, %	C_m
Baseline, new winglet	0 deg	0 deg	——	——	−0.034
Symmetrical inboard	−20 deg	−20 deg	−1.7	2.1	−0.024
Symmetrical outboard	+20 deg	+20 deg	−0.5	1.1	−0.041
Asymmetrical inboard	−20 deg	+20 deg	−0.6	1.2	−0.035
Asymmetrical outboard	+20 deg	−20 deg	0.0	−0.3	−0.041

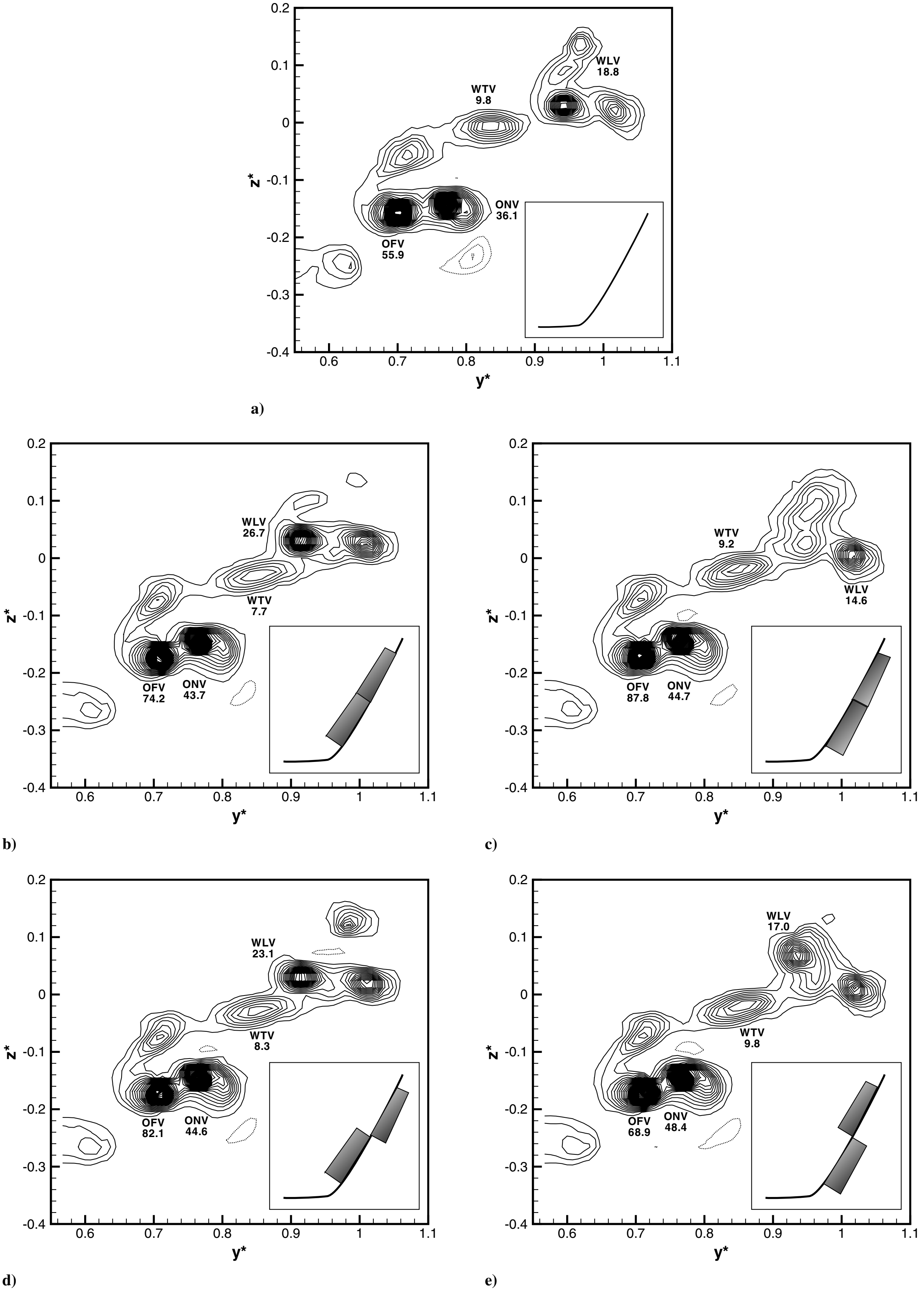

Fig. 13 Contour plots of nondimensional axial vorticity ξ distributions for the configuration with new winglet at $x^* = 0.37, Re_{\bar{c}} = 0.5 \times 10^6, 1 \le \xi \le 50, \triangle\xi = 1$: a) $\delta_u = 0$ deg, $\delta_l = 0$ deg; b) $\delta_u = -20$ deg, $\delta_l = -20$ deg; c) $\delta_u = +20$ deg, $\delta_l = +20$ deg; d) $\delta_u = +20$ deg, $\delta_l = -20$ deg; e) $\delta_u = -20$ deg, $\delta_l = +20$ deg.

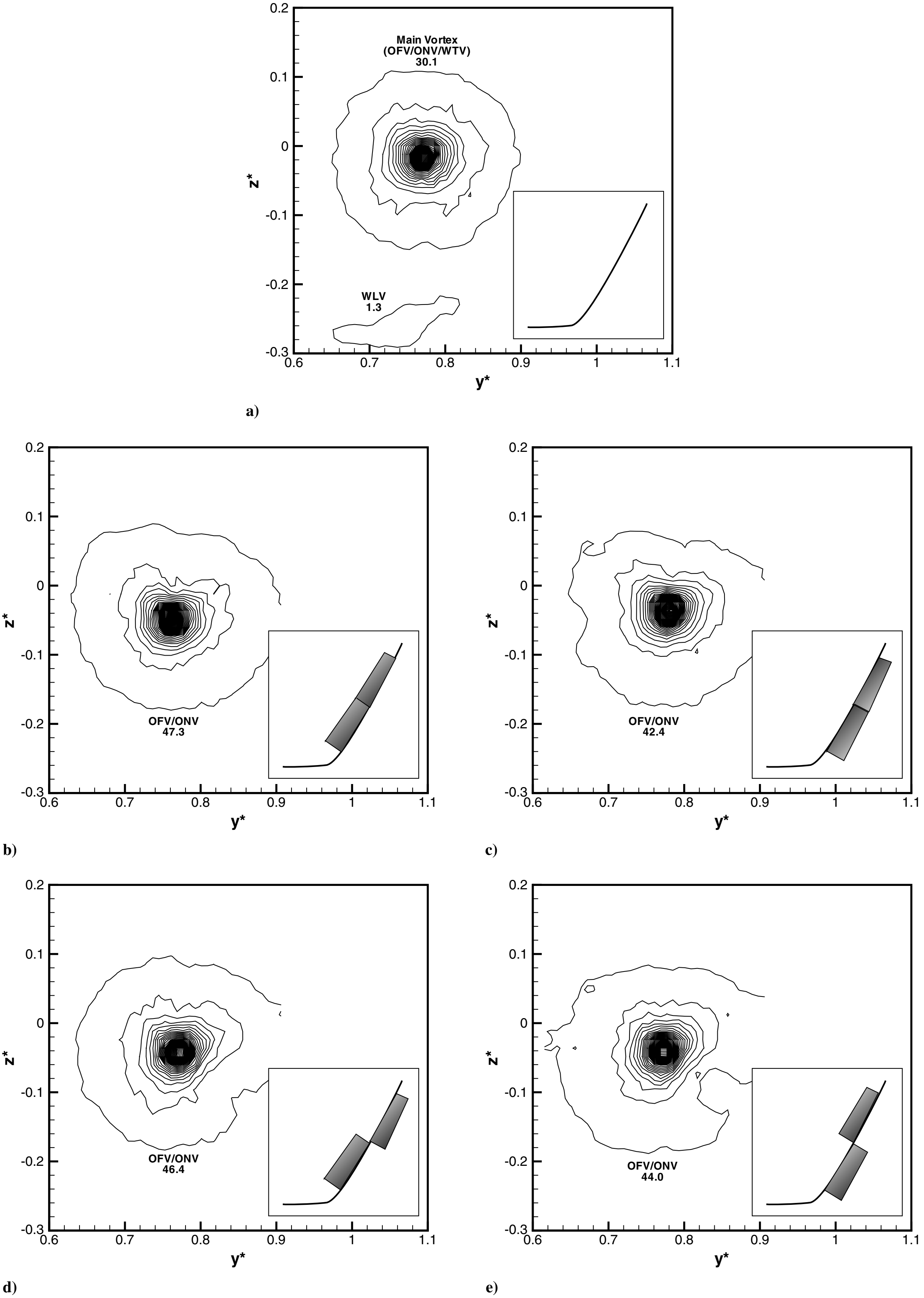

Fig. 14 **Contour plots of nondimensional axial vorticity ξ distributions for the configuration with new winglet at $x^* = 5.6, Re_{\bar{c}} = 0.5 \times 10^6, 1 \leq \xi \leq 50$, $\triangle\xi = 1$: a) $\delta_u = 0$ deg, $\delta_l = 0$ deg; b) $\delta_u = -20$ deg, $\delta_l = -20$ deg; c) $\delta_u = +20$ deg, $\delta_l = +20$ deg; d) $\delta_u = +20$ deg, $\delta_l = -20$ deg; e) $\delta_u = -20$ deg, $\delta_l = +20$ deg.**

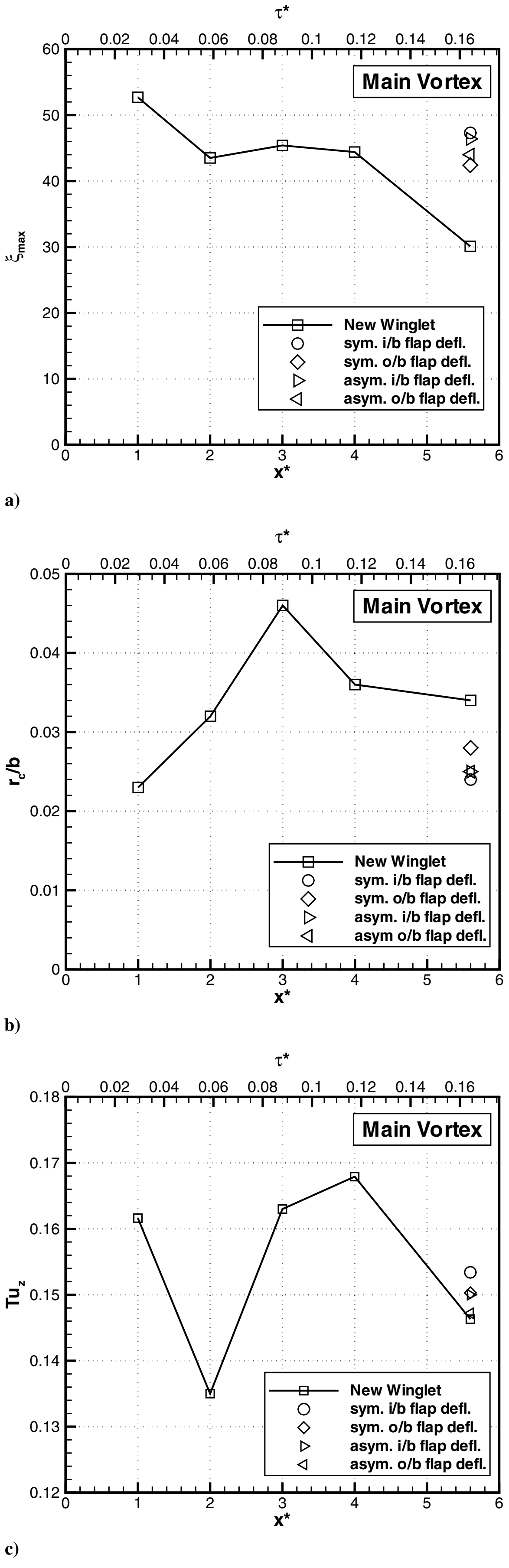

Fig. 15 Development of flowfield variables for the configuration with new winglet between $x^* = 1.0$ and $x^* = 5.6$ for the main vortex, $Re_{\bar{c}} = 0.5 \times 10^6$: a) $\xi_{\max}$, b) r_c/b, c) $Tu_{z,\max}$.

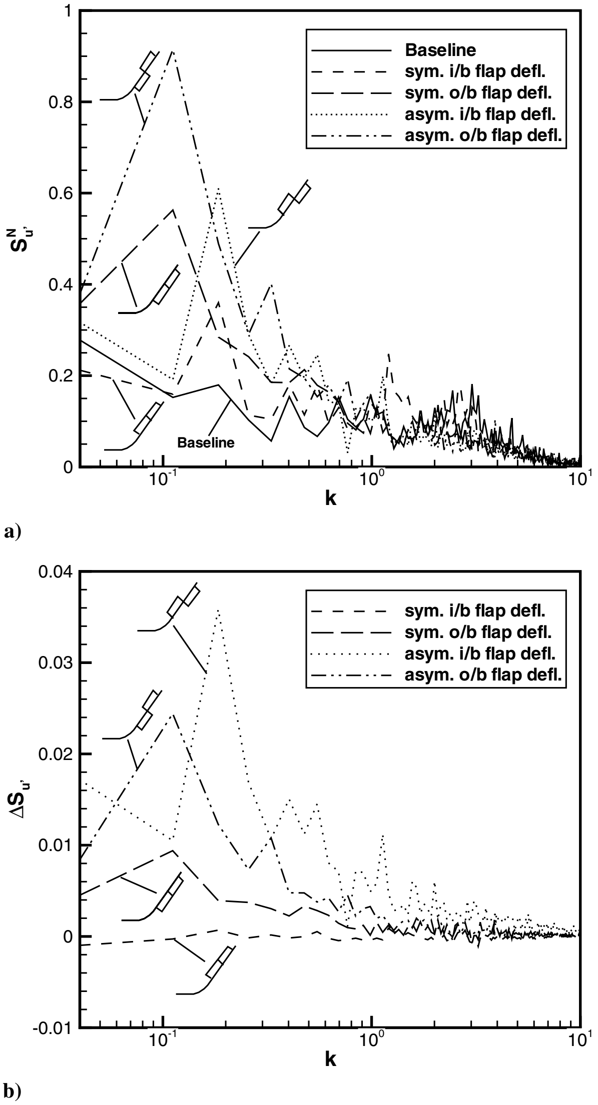

Fig. 16 Comparison of power spectral densities of the axial velocity fluctuations at $x^* = 5.6$ between the case without winglet flap deflection and the cases with symmetrical and asymmetrical deflections: a) normalized, b) difference to the case with no flap deflection.

This instability is related to the strain effect induced by one vortex of a pair on the other one, and appears as a sinusoidal displacement of the vortex trajectories ultimately responsible for the wake vortex collapse in the far field. Regarding two vortex pairs, for example, wing tip vortex and outboard flap vortex, an instability mechanism with both symmetric and asymmetric modes is present, the wavelengths of which are shorter than those of the Crow instability, but large with respect to the effective vortex core size [30]. A typical short-wave instability of the Widnall-type is characterized by a wavelength of the order of the vortex core size, depending also on the internal vortex core structure [18,21]. This instability can also grow in a vortex pair, interfering at the same time with long-wave instabilities.

The wavelength of the Crow-type instability is approximately $\lambda_{\mathrm{Crow}} \approx 8b_0$, $b_0 = 0.76b \div 0.78b$ (cf. Figs. 11 and 14). This wavelength corresponds to a reduced frequency of $k_{\mathrm{Crow}} = f_{\mathrm{Crow}}(b/2)/U_\infty = b/(2\lambda_{\mathrm{Crow}}) \approx 0.08$. It can be seen that the dominant reduced frequencies k_d of the observed spectral density peaks are close to the value of k_{Crow}, thus enhancing a Crow-type instability. The deflection of the winglet flaps leads to a concentration of turbulent kinetic energy in the frequency range of this dominant inherent instability. Analyzing the difference in the spectral densities between the baseline configuration and the configurations with deflected winglet flaps (Fig. 16b), the narrowband amplification produced by the asymmetrical cases is on the order of 20–25. These are the most promising configurations resulting in a strong amplification of the fluctuation level attributed to the long-wave instability responsible for rapid wake vortex decay.

Conclusions and Outlook

An experimental investigation on the wake vortex development of a large transport aircraft in approach configuration fitted with a large winglet and winglet flaps has been performed. A detailed four-engined half-model of 1:32 scale is studied at an angle of attack of 7 deg and a Reynolds number based on the mean aerodynamic chord of 0.5×10^6. Vorticity and turbulence intensity are analyzed for seven crossflow planes of the near and extended near field based on advanced hot-wire anemometry. Spectral density distributions of the axial velocity fluctuations have been evaluated for the most downstream plane located at 5.6 spans behind the model. The effect of influencing the wake vortex through static deflection of winglet trailing-edge flaps is discussed. Four different cases, including inboard and outboard, symmetrical and asymmetrical flap deflections, are tested. The main results of this study are as follows:

1) The wake near field shows seven particular vortices, namely, from outboard to inboard, the winglet vortex (WLV), the wing tip vortex (WTV), the outboard flap vortex (OFV), the outboard and inboard nacelle vortices (ONV and INV), the vortex of the wing-fuselage junction (WFV), and the horizontal tail plane vortex (HTV). These vortices are connected through the vortex sheet shed at the wing trailing edge, except for the HTV. Positive axial vorticity is attributed to WLV, WTV, OFV, ONV, and INV, whereas WFV and HTV show negative axial vorticity. The latter is caused by the negative circulation gradient at the wing-fuselage junction and the negative lift of the horizontal tail plane needed for trimmed flight. The highest level of axial peak vorticity is given by the OFV because of the highly loaded outboard flap. It is located closely to the free circulation centroid which is the wake vortex roll-up center.

2) In the extended near field, the position and strength of the particular vortices change progressively because of the wake roll-up process and vortex merging. This process forms the remaining rolled-up vortex to which most of the vorticity is fed, up to $\tau^* \approx 0.16$. The core regions of the particular wake vortices are characterized by axial vorticity peaks and considerable axial velocity deficits (8–11%). The vortex core structure exhibits maximum turbulence intensities on the order of 12–18%.

3) The deflection of winglet flaps results in additional vortical structures in the wing tip area. The presence of these vortices enhances the merging process of WTV, OFV, and ONV in the near field, and strengthens the interference between WLV and merged WTV/OFV/ONV. Thus, the remaining rolled-up vortex is formed more upstream compared with the noninterfering case. The peak turbulence intensities in the core of the remaining vortex increases by approximately 4%.

4) Spectral analysis of the axial velocity fluctuations performed for the remaining vortex at the most downstream station shows a broadband distribution of turbulent kinetic energy for the baseline configuration, but specific narrowband concentrations for the cases with winglet flap deflection. The most pronounced quasi-periodic fluctuations occur at reduced frequencies of $k \approx 0.1$–0.2, which correspond to the frequency range of the Crow-type instability. The spectral densities reach their highest levels for the cases with asymmetrical flap deflection. With the lower flap deflected inboard, a narrowband amplitude amplification by a factor of 25 occurs. This increase in narrowband fluctuations is thought to promote inherent instabilities contributing to wake vortex collapse.

Future investigations will focus on active flap deflections to further enhance the frequency dependent energy concentrations in the rolled-up vortex amplifying long-wave wake vortex instabilities.

Acknowledgment

The support of these investigations by the German Government, Federal Ministry of Economics and Technology, under contract number 20A0301J is gratefully acknowledged.

References

[1] Hünecke, K., "Structure of a Transport Aircraft-Type Near Field Wake," *The Characterisation & Modification of Wakes from Lifting Vehicles in Fluids*, AGARD CP-584, May 1996, pp. 5-1–5-9.

[2] Brenner, F., "Air Traffic Control Procedures for the Avoidance of Wake Vortex Encounters: Today and Future Developments by Deutsche Flugsicherung GmbH," *The Characterisation & Modification of Wakes from Lifting Vehicles in Fluids*, AGARD CP-584, May 1996, pp. 4-1–4-14.

[3] Gerz, T., "Wake Vortex Prediction and Observation: Towards an Operational System," *Proceedings ODAS 2001, S1-3, ONERA-DLR Aerospace Symposium*, ONERA, Chatillon, France, June 2001, pp. S1-3.1–S1-3.10, ISBN 2-7257-006-X.

[4] Betz, A., "Das Verhalten von Wirbelsystemen," *Zeitschrift für Angewandte Mathematik und Mechanik*, Vol. 12, No. 3, 1932, pp. 164–174.
doi:10.1002/zamm.19320120307

[5] Donaldson, C. duP., and Bilanin, A. J., "Vortex Wakes of Conventional Aircraft," AGARDograph No. 204, May 1975.

[6] Devenport, W. J., Rife, M. C., Liapis, S. I., and Follin, G. J., "The Structure and Development of a Wing-Tip Vortex," *Journal of Fluid Mechanics*, Vol. 312, April 1996, pp. 67–106.
doi:10.1017/S0022112096001929

[7] Spalart, P. R., "Airplane Trailing Vortices," *Annual Review of Fluid Mechanics*, Vol. 30, Jan. 1998, pp. 107–138.
doi:10.1146/annurev.fluid.30.1.107

[8] Rossow, V. J., "Lift-Generated Vortex Wakes of Subsonic Transport Aircraft," *Progress in Aerospace Sciences*, Vol. 35, No. 6, 1999, pp. 507–560.
doi:10.1016/S0376-0421(99)00006-8

[9] Hünecke, K., "From Formation to Decay: Extended-Time Wake Vortex Characteristics of Transport-Type Aircraft," AIAA Paper 2002-3265, June 2002.

[10] Henke, R., "Validation of Wing Technologies on an Airbus A340 Flying Testbed: First Flight Test Results from the European Program AWIATOR," *ICAS Proceedings, 24th Congress of the International Council of the Aeronautical Sciences*, International Council of the Aeronautical Sciences Paper 2004-4.4.1, Sept. 2004.

[11] Coustols, E., Stumpf, E., Jacquin, L., Moens, F., Vollmers, H., and Gerz, T., "Minimised Wake: A Collaborative Research Programme on Aircraft Wake Vortices," AIAA Paper 2003-0938, Jan. 2003.

[12] Gerz, T., Holzäpfel, F., and Darracq, D., "Commercial Aircraft Wake Vortices," *Progress in Aerospace Sciences*, Vol. 38, No. 3, 2002, pp. 181–208.
doi:10.1016/S0376-0421(02)00004-0

[13] Holzäpfel, F., and Robins, R. E., "Probabilistic Two-Phase Aircraft Wake-Vortex Model: Application and Assessment," *Journal of Aircraft*, Vol. 41, No. 5, 2004, pp. 1117–1126.

[14] Köpp, F., Rahm, S., Smalikho, I., Dolfi, A., Cariou, J.-P., Harris, M., and Young, R. I., "Comparison of Wake-Vortex Parameters Measured by Pulsed and Continuous-Wave Lidars," *Journal of Aircraft*, Vol. 42, No. 4, 2005, pp. 916–923.

[15] Winckelmans, G. S., "Vortex Methods," *The Encyclopedia of Computational Mechanics*, edited by E. Stein, R. de Borst, and T. J. R. Hughes, Vol. 3, Wiley, New York, 2004.

[16] Stumpf, E., "Study of Four-Vortex Aircraft Wakes and Layout of Corresponding Aircraft Configurations," *Journal of Aircraft*, Vol. 42, No. 3, 2005, pp. 722–730.

[17] Holzäpfel, F., Hofbauer, T., Darracq, D., Moet, H., Garnier, F., and Gago, C. F., "Analysis of Wake Vortex Decay Mechanism in the Atmosphere," *Aerospace Science and Technology*, Vol. 7, No. 4, 2003, pp. 263–275.
doi:10.1016/S1270-9638(03)00026-9

[18] Breitsamter, C., Bellastrada, C., and Laschka, B., "Investigations on the Turbulent Wake Vortex Flow of Large Transport Aircraft," *ICAS Proceedings, 23rd International Congress of the Aeronautical Sciences*, International Council of the Aeronautical Sciences, ICAS-2002-3.8.2, Sept. 2002, pp. 382.1–382.13.

[19] Elsenaar, A., "Optimum Wing Load Distribution to Minimize Wake Vortex Hazard," *Conference on Capacity and Wake Vortices*, Imperial College London, London, Sept. 2001.

[20] Breitsamter, C., "Beeinflussung des Nachlaufwirbelsystems von Großflugzeugen," *Proceedings DGLR, Symposium: The Airport as a Neighbour. Challenges and Solutions for Future Air Transport Systems*, Deutsche Gesellschaft für Luft- und Raumfarht , Bonn, Germany, Oct. 2004.

[21] Jacquin, L., Fabre, D., Sipp, D., Theofilis, V., and Vollmers, H., "Instabilities and Unsteadiness of Aircraft Wake Vortices," *Aerospace*

Science and Technology, Vol. 7, No. 8, 2003, pp. 577–593.
doi:10.1016/j.ast.2003.06.001

[22] Rennich, S. C., and Lele, S. K., "Method for Accelerating the Destruction of Aircraft Wake Vortices," *Journal of Aircraft*, Vol. 36, No. 2, 1999, pp. 398–404.

[23] Durston, D. A., Walker, S. M., Driver, D. M., Smith, S. C., and Savas, Ö., "Wake Vortex Alleviation Flow Field Studies," *Journal of Aircraft*, Vol. 42, No. 4, 2005, pp. 894–907.

[24] Crouch, J. D., Miller, G. D., and Spalart, P. R., "Active-Control System for Breakup of Airplane Trailing Vortices," *AIAA Journal*, Vol. 39, No. 12, 2001, pp. 2374–2381.

[25] Kauertz, S., and Neuwerth, G., "Excitation of Instabilities in the Wake of an Airfoil with Winglets," *AIAA Journal*, Vol. 45, No. 3, 2007, pp. 577–598.
doi:10.2514/1.26462

[26] Fabre, D., and Jacquin, L., "Stability of a Four-Vortex Aircraft Wake Model," *Physics of Fluids*, Vol. 12, No. 10, 2000, pp. 2438–2443.
doi:10.1063/1.1289397

[27] Breitsamter, C., "Turbulente Strömungsstrukturen an Flugzeugkonfigurationen mit Vorderkantenwirbeln," Dissertation, DM 18432, Technical Univ. of Munich, Verlag Wissenschaft (Aerodynamik), Germany, ISBN 3-89675-201-4, June 1997.

[28] Meunier, P., and Leweke, T., "Three-Dimensional Instability During Vortex Merging," *Physics of Fluids*, Vol. 13, No. 10, 2001, pp. 2747–2750.
doi:10.1063/1.1399033

[29] Crow, S. C., "Stability Theory for a Pair of Trailing Vortices," *AIAA Journal*, Vol. 8, No. 12, 1970, pp. 2172–2179.

[30] Crouch, J. D., "Instability and Transient Growth for Two Trailing-Vortex Pairs," *Journal of Fluid Mechanics*, Vol. 350, Nov. 1997, pp. 311–330.
doi:10.1017/S0022112097007040